Parameter Identification Methods for Multi-Phase Permanent Magnet Synchronous Machines

Michael Hoerner ⓘ*†, Valentin Hoppe†, Timo Wilfling†, Armin Dietz†, Petros Karamanakos ⓘ‡, Ralph Kennel*

*Chair of Electrical Drive Systems and Power Electronics, Technical University of Munich, Germany
†Institute ELSYS, Technische Hochschule Nuremberg, Germany
‡Faculty of Information Technology and Communication Sciences, Tampere University, Finland
Email: michael.hoerner@th-nuernberg.de

Abstract—This paper presents and assesses parameter estimation methods for multi-phase permanent magnet synchronous machines. More specifically, three different methods are considered, namely, a step-response method for identifying the stator resistance and absolute inductance values, a Fourier analysis-based method to obtain the harmonics in the permanent magnet flux-linkage, and a methodology to acquire the flux-linkage maps. To verify the effectiveness of the methods in question, experimental tests based on a six-phase PMSM drive are performed, and the results are compared with those acquired with finite-element-analysis simulations. Finally, to promote open science and make the findings of this work publicly available, all results are published within the open-source *UltraZohm* project.

Index Terms—Open science, parameter identification, multi-phase, PMSM, harmonics, FEA, flux-linkage maps

I. INTRODUCTION

Over the last decades, variable speed drives with multi-phase winding configurations have gained a lot of attention in the scientific community thanks to their fault-tolerant operating capabilities. As a result, they have been increasingly adopted in fault-tolerant applications, such as autonomous driving, more-electric aircraft or decentralized energy conversion [1]. Nevertheless, the aforementioned favorable operation comes at a cost of a more complex description of the electromagnetic behavior of the machine. For the design of model-based control algorithms, such as field oriented control (FOC) or model predictive control (MPC), precise knowledge of the model parameters is crucial. Therefore, effective parameter identification methods are required to ensure successful control of multi-phase machines.

For conventional three-phase permanent magnet synchronous machines (PMSMs), a fundamental-wave model in the rotor-fixed rotating (dq) frame is the common modeling approach [2]. Parameter identification methods for such machines that focus mainly on the identification of the stator resistance, inductances or flux-linkage maps, and permanent magnet (PM) flux-linkage, have already been widely investigated in the literature [3]–[7]. Contrary to this, for multi-phase machines in general, and PMSMs in particular, only a few relevant works have been published [8]–[11]. Besides

that, experimental results have rarely been compared to finite-element-analysis (FEA) simulations to provide a meaningful verification of the computed parameters.

Motivated by the above, this paper provides a detailed description of a parameter identification method for all harmonic subspaces of multi-phase PMSMs based on [10]. By applying the method proposed in [10] to six-phase PMSMs, the model of the machine in question is derived by employing the vector space decomposition (VSD) approach [12] and presented in Section II. Following, Section III introduces methods for the parameter identification of all the sub-systems of six-phase PMSMs. In Section IV, relevant experimental results are presented and compared to an FEA model. It is worth mentioning that the measurement algorithms are implemented using the *UltraZohm*, an open-source rapid-control prototyping platform [13], [14]. The algorithms and the respective measurement results are therefore available to the public. The paper concludes with Section V.

II. MULTI-PHASE PERMANENT MAGNET SYNCHRONOUS MACHINE MODELING

One of the most common approaches for modeling multi-phase machines is the VSD approach [12], which can also be derived from the theory of symmetrical components [15]. It can be interpreted as a generalized form of the Clarke transformation. The VSD transformation matrix $\mathbf{T}_{\mathrm{VSD}}$ is dependent on the geometric distribution of the windings and the number of phases of the machine and decomposes the stator currents into several independent orthogonal subspaces. For the considered six-phase machine shown in Fig. 1 and with its three orthogonal planes, the VSD matrix can be written as

$$\mathbf{T}_{\mathrm{VSD}} = \frac{1}{3}\begin{bmatrix} 1 & -\frac{1}{2} & -\frac{1}{2} & \frac{\sqrt{3}}{2} & -\frac{\sqrt{3}}{2} & 0 \\ 0 & \frac{\sqrt{3}}{2} & -\frac{\sqrt{3}}{2} & \frac{1}{2} & \frac{1}{2} & -1 \\ 1 & -\frac{1}{2} & -\frac{1}{2} & -\frac{\sqrt{3}}{2} & \frac{\sqrt{3}}{2} & 0 \\ 0 & -\frac{\sqrt{3}}{2} & \frac{\sqrt{3}}{2} & \frac{1}{2} & \frac{1}{2} & -1 \\ 1 & 1 & 1 & 0 & 0 & 0 \\ 0 & 0 & 0 & 1 & 1 & 1 \end{bmatrix}. \quad (1)$$

Applying (1) to the natural phase quantities of the stator currents $\mathbf{i}_{\mathrm{s}}^{a1 \to c2} = [i_{a1}\ i_{b1}\ i_{c1}\ i_{a2}\ i_{b2}\ i_{c2}]^T$, results
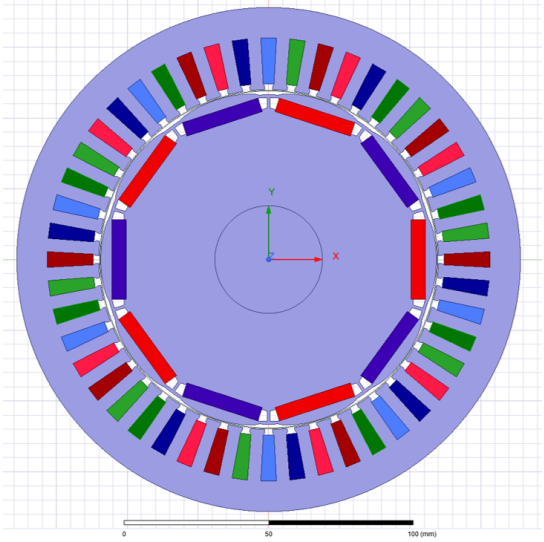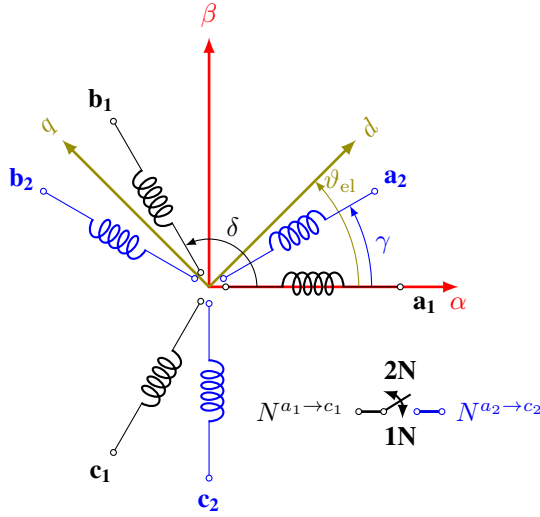
Fig. 1: Left: Winding configuration in the stator- and rotor-fixed coordinate systems with $\delta = \frac{2}{3}\pi$, and $\gamma = \frac{\pi}{6}$. 1N and 2N refer to the two possible neutral point configurations, namely 1N stands for the case where the neutral points of both three-phase winding subsets $N^{a1 \to c1}$ and $N^{a2 \to c2}$ are connected, while 2N for the case where the neutral points are not connected. Right: Cross-section of the six-phase PMSM, showing the winding distribution and rotor geometry of the FEA model.

in the decomposed stator-fixed VSD current components $\mathbf{i}_s{}^{\text{VSD'}} = [i_\alpha\ i_\beta\ i_X\ i_Y\ i_{0+}\ i_{0-}]^T$, given by

$$\mathbf{i}_s{}^{\text{VSD'}} = \mathbf{T}_{\text{VSD}}\mathbf{i}_s{}^{a1 \to c2} . \tag{2}$$

In (2), i_α and i_β relate to the fundamental component of the current as well as the $12k_{\alpha\beta} \pm 1$ harmonics, with $k_{\alpha\beta} = \{1, 2, 3, \ldots\}$, i_X and i_Y to the $6k_{XY} \pm 1$ harmonics, with $k_{XY} = \{1, 3, 5, \ldots\}$ and i_0^+, i_0^- to the $3k_0$ harmonics, with $k_0 = \{1, 3, 5, \ldots\}$. As per [10], using the Park transformation

$$\mathbf{T}_{\text{P}}(\vartheta_{\text{el}}) = \begin{bmatrix} \cos(\vartheta_{\text{el}}) & \sin(\vartheta_{\text{el}}) \\ -\sin(\vartheta_{\text{el}}) & \cos(\vartheta_{\text{el}}) \end{bmatrix}, \tag{3}$$

with the electrical rotor position ϑ_{el} for the $\alpha\beta$ components and $-\vartheta_{\text{el}}$ for the XY components, and applying it to $\mathbf{i}_s{}^{\text{VSD'}}$ results in

$$\mathbf{i}_s{}^{\text{VSD}} = \mathbf{T'}_{\text{P}}(\vartheta_{\text{el}})\mathbf{i}_s{}^{\text{VSD'}} = \begin{bmatrix} \mathbf{T}_{\text{P}}(\vartheta_{\text{el}}) & \mathbf{0}_2 & \mathbf{0}_2 \\ \mathbf{0}_2 & \mathbf{T}_{\text{P}}(-\vartheta_{\text{el}}) & \mathbf{0}_2 \\ \mathbf{0}_2 & \mathbf{0}_2 & \mathbf{I}_2 \end{bmatrix} \mathbf{i}_s{}^{\text{VSD'}}, \tag{4}$$

where $\mathbf{i}_s{}^{\text{VSD}} = [i_d\ i_q\ i_x\ i_y\ i_{0+}\ i_{0-}]^T$. With the current components in the transformed space, the machine model can be written as [10]

$$\mathbf{u}_s^{dq} = R_s\mathbf{i}_s^{dq} + \omega_{\text{el}}\mathbf{J}\boldsymbol{\psi}_s^{dq} + \frac{\mathrm{d}}{\mathrm{d}t}\boldsymbol{\psi}_s^{dq} \tag{5a}$$

$$\mathbf{u}_s^{xy} = R_s\mathbf{i}_s^{xy} - \omega_{\text{el}}\mathbf{J}\boldsymbol{\psi}_s^{xy} + \frac{\mathrm{d}}{\mathrm{d}t}\boldsymbol{\psi}_s^{xy} \tag{5b}$$

$$\mathbf{u}_s^0 = R_s\mathbf{i}_s^0 + \frac{\mathrm{d}}{\mathrm{d}t}\boldsymbol{\psi}_s^0, \tag{5c}$$

where $\mathbf{u}_s^\square$ are the decomposed stator voltages, R_s is the per-phase stator resistance, $\mathbf{J} = \begin{bmatrix} 0 & -1 \\ 1 & 0 \end{bmatrix}$, ω_{el} is the electrical rotational speed, and $\boldsymbol{\psi}_s^\square$ are the decomposed flux-linkages.

Depending on the machine under consideration, $\boldsymbol{\psi}_s^\square$ can be modeled using absolute inductances or differential inductances. Low-order harmonics of the PM flux-linkage can also be considered.

III. PARAMETER IDENTIFICATION METHODS

In this section the parameter identification methods under discussion are presented. The first method identifies the stator resistance and absolute inductances by examining the current response to a voltage step in the respective axis. For this method a fundamental-wave model with constant machine parameters is sufficient, while saturation and cross-coupling effects are neglected. The second method obtains the low-order PM flux-linkage harmonic parameters. Moreover, when saturation and cross-coupling need to be respected, methods for measuring the flux-linkage maps for each subspace are also presented. Finally, FEA approaches that compute the aforementioned parameters are briefly discussed as they are used for benchmarking purposes.

A. Step Response Method

As presented in [5] for the quantities in the dq-subsystem, the phase resistance R_s and inductances $L_s^\square$ can be identified when applying a voltage step in the respective axis. This is done through curve-fitting of a function to the measured current response using the Levenberg-Marquardt (LM) solver. This method can also be used for the xy- and 0-subsystems when operating the machine in 1N configuration by applying proper voltage steps such that the respective currents are excited.

In this work, the aforementioned approach is employed to estimate the parameters in question. To this end, a voltage step is applied in the axis of interest by means of a two-level

voltage-source inverter (VSI) while having the rotor d-axis aligned with the stator α-axis. Following, the measured current responses are compared with the results acquired by solving the differential equation of the respective voltages, i.e.,

$$\hat{i}_{\mathrm{s}}^{\square}(t) = \frac{u_{\mathrm{s}}^{\square}}{\hat{R}_{\mathrm{s}}} \left(1 - \mathrm{e}^{-\frac{\hat{R}_{\mathrm{s}} \cdot t}{\hat{L}_{\mathrm{s}}^{\square}}}\right), \qquad (6)$$

where $\hat{i}_{\mathrm{s}}^{\square}(t)$ is the estimated current step response, $u_{\mathrm{s}}^{\square}$ is the applied voltage in the respective subspace, e is the Euler number, t is the time, while $\hat{R}_{\mathrm{s}}$ and $\hat{L}_{\mathrm{s}}^{\square}$ are the estimated phase resistance and inductances, respectively. The latter are eventually calculated by minimizing the error between the solution of (6) and the measured step response with the help of the aforementioned LM-algorithm. A more detailed description of this approach can be found in [5].

B. Permanent Magnet Flux-Linkage And Harmonics

For obtaining the permanent magnet (PM) flux-linkage the machine is externally driven at constant speed by a load machine. The phase voltages are measured and analyzed by means of discrete Fourier transformation (DFT). In doing so, the PM flux-linkage amplitudes of the fundamental and the dominant low-order harmonic components, namely, the 3rd, 5th, 7th and 9th, are found. Following, each harmonic PM flux-linkage amplitude is calculated with

$$\psi_{\mathrm{pm}}^{h} = \frac{\hat{u}_{\mathrm{s}}^{h,a1\to c2}}{h\omega_{\mathrm{el}}}, \qquad (7)$$

where ψ_{pm}^{h} and $\hat{u}_{\mathrm{s}}^{h,a1\to c2}$ are the amplitudes of the h-th harmonic of the PM flux-linkage and measured voltage, respectively.

C. Flux-Linkage Map Identification

Besides the resistance and absolute inductance values identified by the step-response method (see Section III-A), it is desirable to identify the flux-linkage maps. This is particularly important when nonlinear machines are of interest as well as when cross-coupling and saturation effects need to be respected. The basic idea of the identification procedure can be found in [10].

1) dq Flux-Linkages: In the dq-subspace, currents are mainly controlled by a proportional-integral (PI) controller. Since imbalance between the two three-phase subsets leads to a 2nd-order current harmonic, [10] proposes an additional resonant (R) controller to compensate for it. Fig. 2 shows the structure of the PIR controller in the dq-frame. With the help of the load machine that keeps the rotational speed constant, different set-points for the dq-currents are set such that the entire operating range of the machine is covered. Subsequently, the resulting voltage $\mathbf{u}_{\mathrm{s}}^{dq}$ and current $\mathbf{i}_{\mathrm{s}}^{dq}$ are measured at each operating point along with the electrical frequency ω_{el}. In a last step, the dq flux linkages are computed with

$$\boldsymbol{\psi}_{s}^{dq} = \frac{\mathbf{J}^{-1}}{\omega_{\mathrm{el}}}(\mathbf{u}_{\mathrm{s}}^{dq} - R_s\mathbf{i}_{\mathrm{s}}^{dq}). \qquad (8)$$
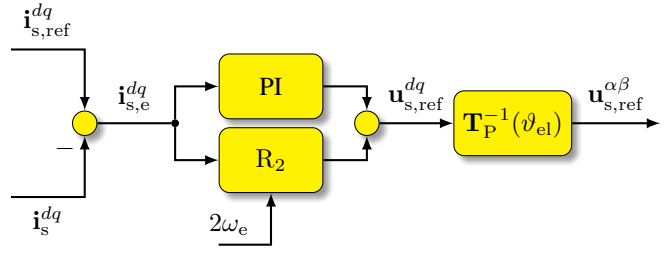

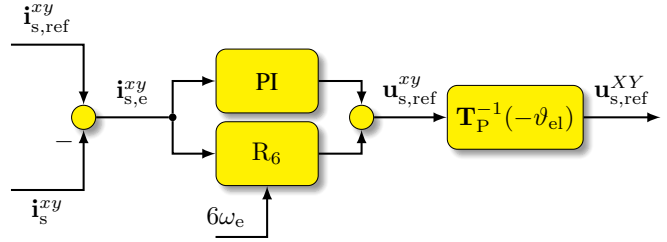Fig. 2: Control structure for dq-subspace flux-linkage identification.

Fig. 3: Control structure for xy-subspace flux-linkage identification.

Note that the above-mentioned measurement campaign needs to be performed at a constant machine temperature to ensure that the stator resistance R_s does not change, and thus bias the results of (8).

2) xy Flux-Linkages: Assuming that the 5th and 7th current harmonics are dominant, a PIR controller according to Fig. 3 is employed. In the xy-subspace, the resonant controller compensates for the non-sinusoidal PM-flux linkage effects. Since this subspace rotates with $-\vartheta_{\mathrm{el}}$, the R-component of the controller is set for $6\omega_{\mathrm{el}}$. This way, both, the 5th and 7th current harmonics are effectively compensated for. As for the PI-component of the controller, it controls the xy-current vector over the whole operating range of the machine. The flux-linkage $\boldsymbol{\psi}_{\mathrm{s}}^{xy}$ is then calculated based on the corresponding measured voltages and currents, i.e.,

$$\boldsymbol{\psi}_{s}^{xy} = -\frac{\mathbf{J}^{-1}}{\omega_{\mathrm{el}}}(\mathbf{u}_{\mathrm{s}}^{xy} - R_s\mathbf{i}_{\mathrm{s}}^{xy}), \qquad (9)$$

where $\mathbf{u}_{\mathrm{s}}^{xy}$, $\mathbf{i}_{\mathrm{s}}^{xy}$, and ω_{el} are the measured quantities.

3) Zero Flux-Linkages: For creating the zero-subspace flux-linkage maps, the stator winding terminals have to be connected as shown in Fig. 4. This allows for the independent control of the i_{s}^{0+} and i_{s}^{0-} currents [10]. Since the 3rd harmonic is the dominant component of the PM flux-linkage in this configuration, the zero-subspace coordinate system is rotated at $3\omega_{\mathrm{el}}$. Similarly to the dq- and xy-subspaces, this enables the control of the current over the entire operating range by means of a PI-controller. Moreover, this controller is augmented with an R-component to compensate for higher-order triplen current harmonics, see Fig. 5. In line with the previous subspaces, the flux-linkage in this subspace is calculated with

$$\boldsymbol{\psi}_{s}^{0} = \frac{\mathbf{J}^{-1}}{3\omega_{\mathrm{el}}}(\mathbf{u}_{\mathrm{s}}^{0} - R_s\mathbf{i}_{\mathrm{s}}^{0}). \qquad (10)$$
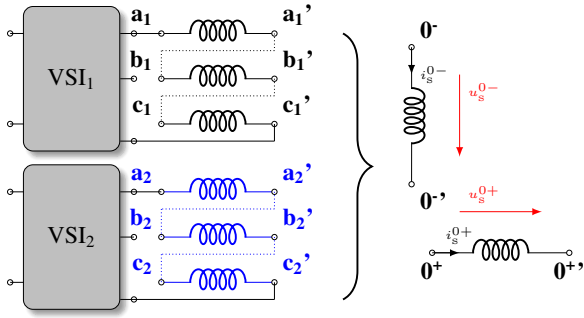
Fig. 4: Terminal configuration for zero-subspace flux-linkage identification.
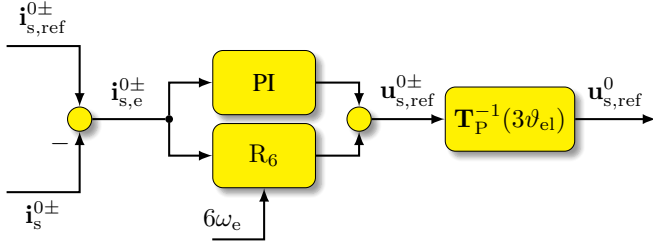

Fig. 5: Control structure for zero-subspace flux-linkage identification.

D. FEA model

To compare and validate the performance of the above-mentioned identification techniques, an FEA model is employed. The model determines the flux-linkage maps at different load points in all considered systems. The FEA model, shown in Fig. 1, is designed with ideal current excitation to eliminate current harmonics and their effects on the flux-linkage calculation. With the inverted VSD matrix $\mathbf{T}_{\mathrm{VSD}}^{-1}$, it is possible to define specific load points in the dq, xy or 0^+0^--subsystem and calculate the corresponding values of $\mathbf{i}_{\mathrm{s}}^{a1 \rightarrow c2} = [i_{a1}\ i_{b1}\ i_{c1}\ i_{a2}\ i_{b2}\ i_{c2}]^T$. The mechanical rotor position in the 2D magneto static FEA design is varied over one electrical period to analyze the harmonics and cross-coupling effects in each subsystem. For generating the flux-linkage maps, the mean value in each axis is computed over one electrical period. During the map calculation in one subsystem, the current values in the other two must be set to zero. This is required as, e.g., due to the magnetic saturation in the stator a current excitation in the xy-subsystem leads to a distorted magnetic field, and thus to a change of the flux-linkage in the dq-subsystem.

IV. EXPERIMENTAL RESULTS

A. Experimental Test Setup

Laboratory-based experiments were conducted using the motor testbench shown in Fig. 6. A speed-controlled induction machine serves as the load machine. The controlled six-phase PMSM is driven by two three-phase, two-level inverters with an Infineon 828-XCC silicon-carbide intelligent power-module (SiC-IPM). The dc-link supply is provided by a bi-

Fig. 6: Lab testbench: 1: *UltraZohm*, 2: Load machine, 3: Six-Phase PMSM, 4: Two-level SiC-inverters, 5: Host computer, 6: Graphical user interface

directional lab power supply. Each inverter is equipped with phase- and dc-link-voltage measurement as well as phase- and dc-current measurement using Sensitec CAS5015SRA tunnel-magneto-resistive current sensors. The voltage measurements are low-pass filtered with a cut-off frequency of $2\,\mathrm{kHz}$, which is accounted for in all calculations. All measuring signals are transmitted differentially to the employed rapid control prototyping platform, i.e., *UltraZohm* [13], and converted by the 16-bit ADCs LTC2311. The six-phase PMSM has PT100 temperature sensors mounted on each phase of the stator winding that are evaluated using a temperature adapter board with LTC2983 measurement ICs. The rotor speed and position feedback are measured by means of a resolver. Finally, the gate and temperature signals of the SiC-IPM are transmitted through optical fibers. All the testbench parameters are shown in Table I. As for the current controller, the PI part with transfer function

$$\frac{Y(s)}{E(s)} = K_{\mathrm{p}} + \frac{K_{\mathrm{i}}}{s}, \tag{11}$$

is implemented on the *UltraZohm*. In the above expression, $Y(s)$ is the controller output, $E(s)$ is the deviation of the controlled variable, K_{p} is the proportional gain, K_{i} is the integral gain and s is the complex Laplace frequency domain parameter. As for the R-component of the controller, described by

$$\frac{Y(s)}{E(s)} = \frac{K_{\mathrm{r}}s}{s^2 + \omega_{\mathrm{R}}^2}, \tag{12}$$

is implemented by impulse invariant discretization. In (12), K_{r} is the proportional gain and ω_{R} is the resonant frequency. All controller gains are presented in Table II.

B. FEA and Testbench Results

This section presents and compares the results acquired via FEA simulations and experimental tests.

TABLE I: Testbench parameters

Parameter	Symbol	Value	Unit
Sampling frequency	f_s	10	kHz
Switching frequency	f_sw	10	kHz
Gate signal interlock time	t_d	300	ns
Mechanical rotor speed for measurements	n_set	1200	min^{-1}
Dc-link voltage	v_dc	565	V
Rated stator current	$i_\text{s,ampl,r}$	10	A
Rated rotor speed	n_r	3000	min^{-1}
Rated torque	M_r	28	N m

TABLE II: Controller gains

Subspace	PI		R	
	$K_\text{p}(\Omega)$	$K_\text{i}(\frac{\Omega}{s})$	$K_\text{r}(\Omega)$	$\omega_\text{R}(\frac{rad}{s})$
dq	10	1500	1000	$2\omega_\text{el}$
xy	15	500	1000	$6\omega_\text{el}$
$zero$	15	100	500	$6\omega_\text{el}$

Heuristically tuned controller gains

1) Step-Response Method: Fig. 7 shows the step responses of i_s^d and i_s^y from the experimental setup. The machine is operated in 1N configuration to also allow for currents in the zero-subsystem and thus render the step-response identification there possible. Prior to applying a voltage step in the q-axis, the rotor is locked to ensure that it is standing still. The presented results in Fig. 7 also show the estimated current $\hat{i}_\text{s}^\square$ (see (6)) after the optimization with the LM-algorithm. As can be seen, the results of the optimization are very accurate with $R^2 \geq 0.9998$ for all evaluated step responses. Moreover, the resulting stator resistance and absolute inductance values are shown in Table III. Therein, comparisons with the absolute inductance values calculated from flux-linkage maps—obtained from the FEA simulations in Fig. 9 and discussed in Section IV-B3—are also provided.

2) PM Flux-Linkage Harmonics: For the measurement of the PM flux-linkage harmonics, the switches of the inverters are in tri-state mode and the six-phase PMSM is kept at constant speed by the load machine. By measuring the induced voltage at each phase and the rotational speed, the fundamen-

TABLE III: Estimated machine parameters from the step-response method compared with FEA results

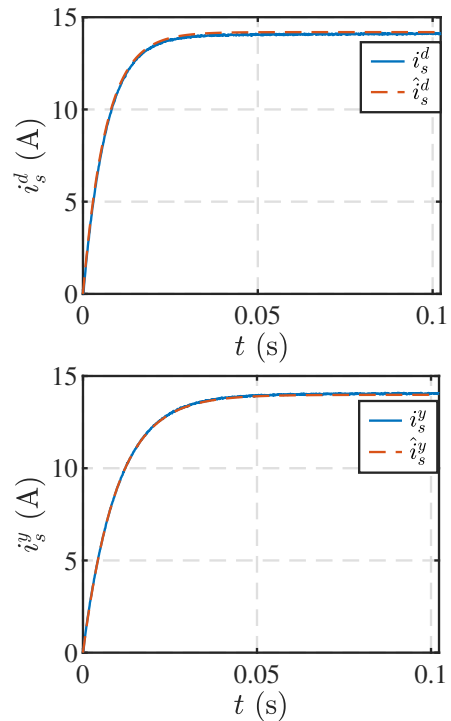| Parameter	Symbol	Step-Response	FEA	Unit
Winding resistance	R_s	0.27		Ω
d-Axis inductance	L_s^d	1.74	1.84	mH
q-Axis inductance	L_s^q	3.80	4.15	mH
x-Axis inductance	L_s^x	2.80	2.87	mH
y-Axis inductance	L_s^y	2.65	2.89	mH
0+ -Axis inductance	L_s^{0+}	1.53	1.57	mH
0- -Axis inductance	L_s^{0-}	1.20	1.59	mH

Fig. 7: Measured step responses of i_s^d (top) and i_s^y (bottom). The blue lines show the measured currents, while the red lines show those estimated with (6) after the LM-optimization.

TABLE IV: Permanent magnet flux-linkage

Harmonic Order	Symbol	Testbench	FEA	Unit
Fundamental	ψ_pm^1	194	197	mV s
3rd	ψ_pm^3	5	4	mV s
5th	ψ_pm^5	0.8	0.7	mV s
7th	ψ_pm^7	0.6	0.4	mV s
9th	ψ_pm^9	0.3	0.1	mV s

tal and harmonic components of the PM flux-linkages are computed with (7). The results are presented in Table IV and compared with those from the FEA simulations. With regards to the fundamental component ψ_pm^1, the results match very closely, demonstrating the effectiveness of the estimation method. As for the harmonics, their amplitude is very low in the specific machine, with the dominant harmonic being the 3rd one, the amplitude of which is only 2% of the fundamental component. As a result, measuring the harmonics in the specific experimental setup is challenging. This becomes even more difficult as the range and resolution of the voltage measurement circuitry of the inverter is designed for 900 V. Therefore, high deviations in the results are anticipated and fully justified. Nevertheless, the discussed method can accurately estimate the harmonics as well, as shown in [10] where the PMSM under test had pronounced harmonics in the PM flux-linkage.

3) Flux-Linkage Maps: The flux-linkage maps for each subspace are measured at a constant speed and machine

TABLE V: Flux-linkage maps comparison

Symbol	RMSD (mVs)
ψ_{s}^{d}	1.79
ψ_{s}^{q}	2.38
ψ_{s}^{x}	1.78
ψ_{s}^{y}	2.13
ψ_{s}^{0+}	1.54
ψ_{s}^{0-}	1.59

temperature of $40\,^{\circ}\mathrm{C}$. In order to heat up the machine, the current reference $\mathbf{i}_{\mathrm{s,ref}}^{dq}$ is set to $(-i_{\mathrm{s,ampl,r}}, i_{\mathrm{s,ampl,r}})^{T}$ until the desired winding temperature is reached. If during the measurement procedure, the temperature rises above $45\,^{\circ}\mathrm{C}$ the current reference $\mathbf{i}_{\mathrm{s,ref}}^{dq}$ is set to $(0\,\mathrm{A}, 0\,\mathrm{A})^{T}$ and experiment is paused until the winding temperature is within the temperature hysteresis band of $5\,^{\circ}\mathrm{C}$. An automated measurement process ensures this. The stator resistance determined by the step-response method in conjunction with the measured temperature is tracked during the flux-linkage map measurement. This allows accounting for the ohmic voltage drop in (8), (9), and (10), while considering the correct stator resistance value.

Within the context of this experiment, the voltages, currents and electrical frequency are measured. The flux-linkage value for every current combination is calculated along with the currently effective stator resistance. For the specific machine under consideration, the flux-linkage maps are measured with a grid step-size of $2.5\,\mathrm{A}$, within the range $\pm i_{\mathrm{s,ampl,r}}$. This results in 81 operating points that must be measured for each subspace. The testbench results are shown in Fig. 8. For the FEA, all the operating points for computing flux-linkage maps of all subspaces are simulated. The resulting phase flux-linkages are then decomposed to their VSD components with the help of (2) and (4) to obtain the results shown in Fig. 9. To better assess the differences between the FEA and experimental results, the root-mean-square deviation (RMSD), i.e.,

$$RMSD_{\psi_{\mathrm{s}}^{\square}} = \sqrt{\frac{\sum_{i=1}^{81}\left(\psi_{\mathrm{s,FEA}}^{\square} - \psi_{\mathrm{s,Testbench}}^{\square}\right)^{2}}{81}}, \quad (13)$$

over all 81 operating points of each flux-linkage map serves as a performance metric, see Table V. As can be seen, the averaged RMSD of each flux-linkage map is quite low, indicating that the accuracy of the experimentally generated maps are reasonably accurate. Therefore, it can be concluded that the method in question can be successfully used with six-phase PMSMs and deal with second-order phenomena, such as cross-coupling and saturation, that arise in a real-world setting.

V. Conclusion

This paper presented a comparison of estimated machine parameters resulted from FEA simulations and experimental tests at the example of a six-phase PMSM. The results showed that the examined parameter identification methods are able to compute the parameters of multi-phase PMSMs from in-system measurements at comparable precision with the FEA. The stator resistance, all subsystem flux-linkage maps, inductances, and low-order harmonics of the PM flux-linkage were successfully identified with an overall deviation below 10%. Moreover, these results, such as the flux-linkage maps, can be further exploited to deduce other machine parameters, e.g., the absolute and/or differential inductances. Finally, it is worth mentioning that in an attempt to promote open science, the presented results are available to the scientific community as they are published within the scope of the open-source project *UltraZohm*.

References

[1] E. Levi, "Multiphase electric machines for variable-speed applications," *IEEE Trans. Ind. Electron.*, vol. 55, no. 5, pp. 1893–1909, May 2008.

[2] D. Schröder, *Elektrische Antriebe - Regelung von Antriebssystemen.* Berlin, Heidelberg: Springer, 2015.

[3] K. Rahman and S. Hiti, "Identification of machine parameters of a synchronous motor," in *Proc. IEEE Ind. Appl. Soc. Annu. Mtg.*, vol. 1, Salt Lake City, UT, USA, Oct. 2003, pp. 409–415.

[4] S. L. Kellner and B. Piepenbreier, "General PMSM d,q-model using optimized interpolated absolute and differential inductance surfaces," in *Proc. IEEE Int. Elect. Mach. Drives Conf.*, Niagara Falls, ON, Canada, May 2011, pp. 212–217.

[5] M. Hoerner, S. Wendel, and A. Dietz, "Automated parameter identification of fractional horse power permanent magnet synchronous motors," in *Proc. Innov. Small Drives and Micro-Motor Sys.*, Saarbruecken, Germany, Sep. 2017, pp. 1–6.

[6] S. Wendel, P. Karamanakos, P. Gebhardt, A. Dietz, and R. Kennel, "Flux linkage-based direct model predictive current control for synchronous machines," *IEEE Trans. Power Electron.*, vol. 36, no. 12, pp. 14 237–14 256, Dec. 2021.

[7] S. Wiedemann and C. M. Hackl, "Simultaneous identification of inverter and machine nonlinearities for self-commissioning of electrical synchronous machine drives," *IEEE Trans. Energy Convers.*, pp. 1–14, 2023, in press, DOI: 10.1109/TEC.2023.3263353.

[8] A. Tessarolo, S. Mohamadian, and M. Bortolozzi, "A new method for determining the leakage inductances of a nine-phase synchronous machine from no-load and short-circuit tests," *IEEE Trans. Energy Convers.*, vol. 30, no. 4, pp. 1515–1527, Dec. 2015.

[9] M. Zabaleta, E. Levi, and M. Jones, "Dual three-phase pm generator parameter identification using experimental and simulated system responses," in *Proc. Int. Symp. Power Electron.*, Novi Sad, Serbia, Oct. 2017, pp. 1–6.

[10] H. M. Eldeeb, A. S. Abdel-Khalik, and C. M. Hackl, "Dynamic modeling of dual three-phase IPMSM drives with different neutral configurations," *IEEE Trans. Ind. Electron.*, vol. 66, no. 1, pp. 141–151, Jan. 2019.

[11] A. Perera and R. Nilsen, "Online identification of six-phase IPMSM parameters using prediction-error sensitivities to model parameters," in *Proc. Int. Power Electron. Conf.*, Himeji, Japan, May 2022, pp. 1225–1232.

[12] Y. Zhao and T. Lipo, "Space vector PWM control of dual three-phase induction machine using vector space decomposition," *IEEE Trans. Ind. Appl.*, vol. 31, no. 5, pp. 1100–1109, Sep./Oct. 1995.

[13] S. Wendel, A. Geiger, E. Liegmann, D. Arancibia, E. Durán, T. Kreppel, F. Rojas, F. Popp-Nowak, M. Diaz, A. Dietz, R. Kennel, and B. Wagner, "UltraZohm - a powerful real-time computation platform for MPC and multi-level inverters," in *Proc. IEEE Int. Symp. Pred. Control of Elect. Drives and Power Electron.*, Quanzhou, China, May/Jun. 2019, pp. 1–6.

[14] E. Liegmann, T. Schindler, P. Karamanakos, A. Dietz, and R. Kennel, "UltraZohm—An open-source rapid control prototyping platform for power electronic systems," in *Proc. Int. Aegean Conf. on Elect. Mach. and Power Electron. & Int. Conf. on Optim. of Elect. and Electron. Equip.*, Brasov, Romania, Sep. 2021, pp. 445–450.

[15] A. A. Rockhill and T. A. Lipo, "A generalized transformation methodology for polyphase electric machines and networks," in *Proc. IEEE Int. Elect. Mach. Drives Conf.*, Coeur d'Alene, ID, USA, May 2015, pp. 27–34.
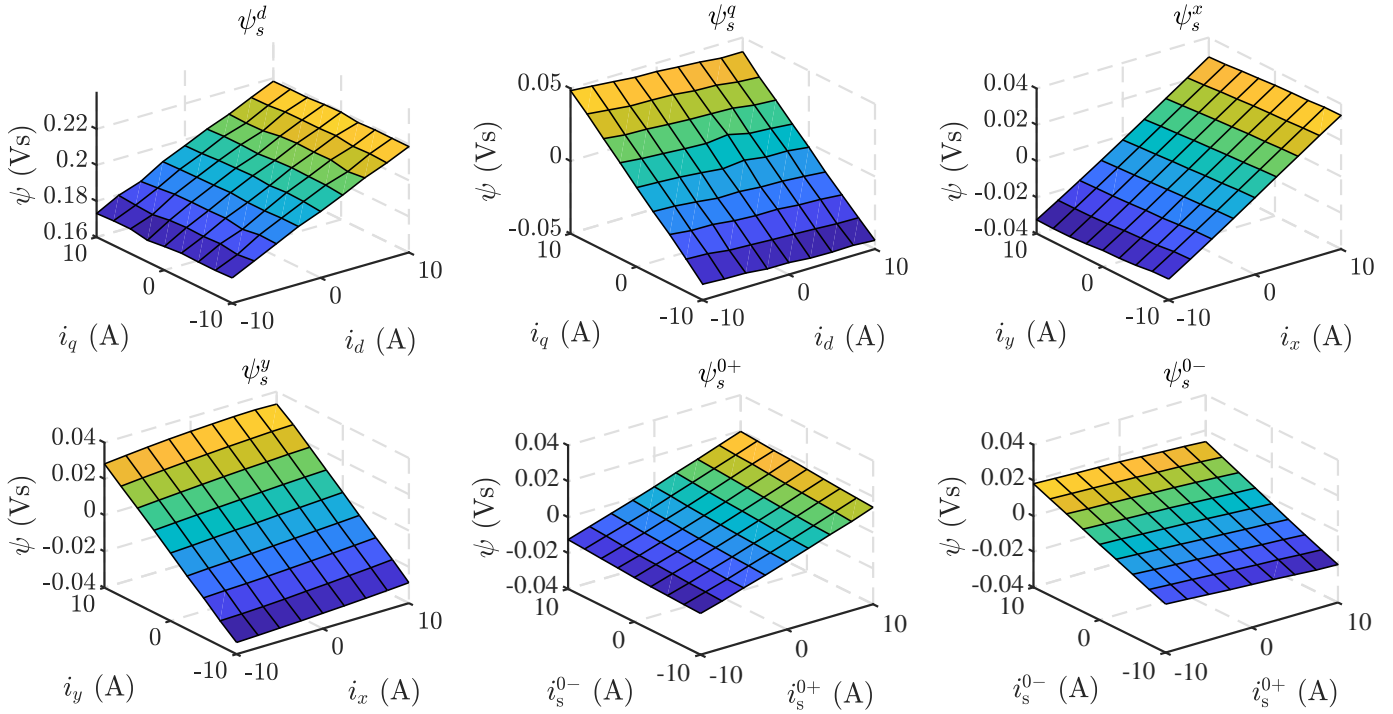
Fig. 8: Testbench results for the flux-linkages ψ_s^d, ψ_s^q, ψ_s^x, ψ_s^y, ψ_s^{0+} and ψ_s^{0-}.
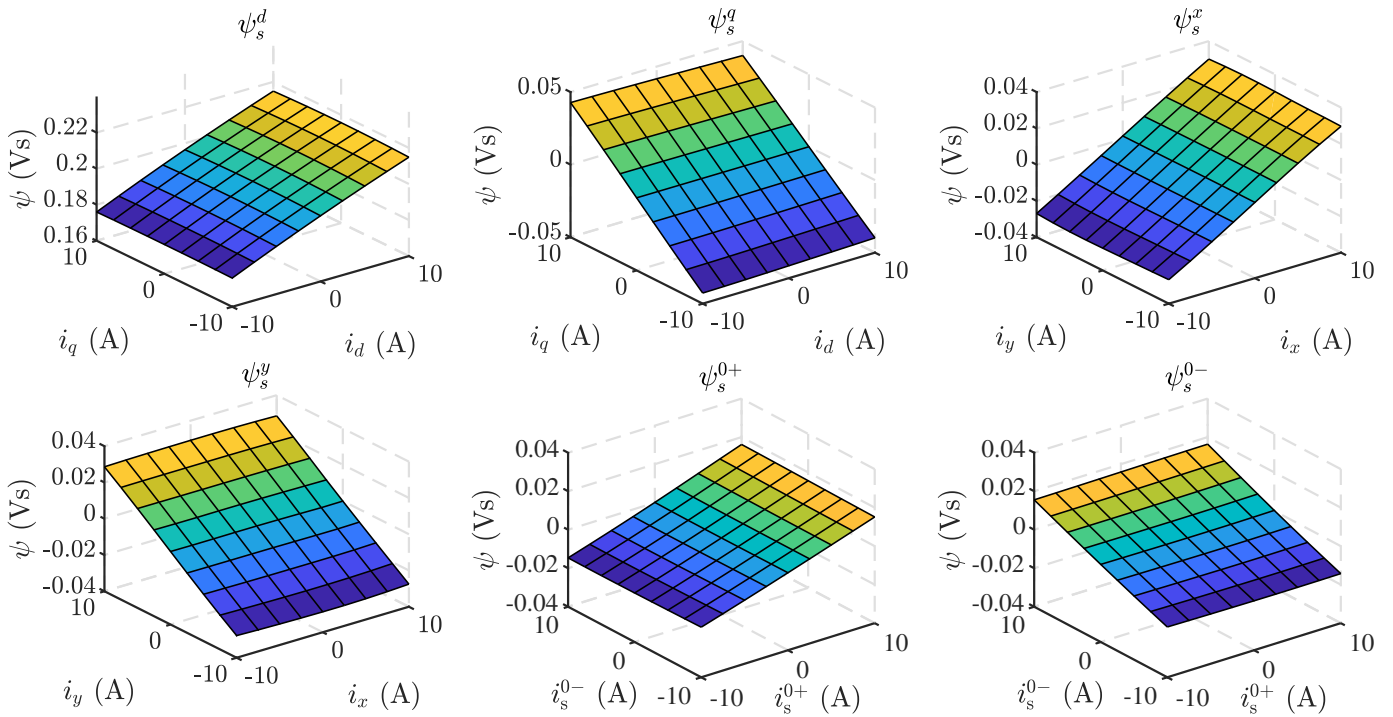
Fig. 9: FEA results for the flux-linkages ψ_s^d, ψ_s^q, ψ_s^x, ψ_s^y, ψ_s^{0+} and ψ_s^{0-}.